

UC Berkeley

UC Berkeley Previously Published Works

Title

Reactive high-spin iron(IV)-oxo sites through dioxygen activation in a metal–organic framework

Permalink

<https://escholarship.org/uc/item/3rg087mt>

Journal

Science, 382(6670)

ISSN

0036-8075

Authors

Hou, Kaipeng

Börgel, Jonas

Jiang, Henry ZH

et al.

Publication Date

2023-11-03

DOI

10.1126/science.add7417

Copyright Information

This work is made available under the terms of a Creative Commons Attribution-NonCommercial License, available at <https://creativecommons.org/licenses/by-nc/4.0/>

Peer reviewed

Title: Reactive high-spin iron(IV)-oxo sites through dioxygen activation in a metal–organic framework

Authors: Kaipeng Hou^{1,2†}, Jonas Börgel^{1,2†}, Henry Z. H. Jiang¹, Daniel J. SantaLucia^{3,4}, Hyunchul Kwon¹, Hao Zhuang^{5,6}, Khetpakorn Chakarawet^{7‡}, Rachel C. Rohde¹, Jordan W. Taylor¹, Chaochao Dun⁸, Maria V. Paley^{1,2}, Ari B. Turkiewicz¹, Jesse G. Park^{1§}, Haiyan Mao⁵, Ziting Zhu^{2,6}, E. Ercan Alp⁹, Jiyong Zhao⁹, Michael Y. Hu⁹, Barbara Lavina^{9,10}, Sergey Peredkov³, Xudong Lv¹, Julia Oktawiec¹¹, Katie R. Meihaus¹, Dimitrios A. Pantazis⁴, Marco Vandone¹², Valentina Colombo¹², Eckhard Bill³, Jeffrey J. Urban^{2,8}, R. David Britt⁷, Fernande Grandjean¹³, Gary J. Long¹³, Serena DeBeer³, Frank Neese⁴, Jeffrey A. Reimer^{2,5}, Jeffrey R. Long^{1,2,5*}

Affiliations:

¹Department of Chemistry, University of California, Berkeley, CA 94720, USA.

²Materials Sciences Division, Lawrence Berkeley National Laboratory, Berkeley, CA 94720, USA.

³Max Planck Institute for Chemical Energy Conversion, Mülheim an der Ruhr D-45470, Germany.

⁴Max-Planck-Institut für Kohlenforschung, Mülheim an der Ruhr D-45470, Germany.

⁵Department of Chemical and Biomolecular Engineering, University of California, Berkeley, CA 94720, USA.

⁶Department of Materials Science and Engineering, University of California, Berkeley, CA 94720, USA.

⁷Department of Chemistry, University of California, Davis, CA 95616, USA.

⁸The Molecular Foundry, Lawrence Berkeley National Laboratory, Berkeley, CA 94720, USA.

⁹Advanced Photon Source, Argonne National Laboratory, Lemont, IL 60439, USA.

¹⁰Center for Advanced Radiation Sources, The University of Chicago, Chicago, IL 60637, USA.

¹¹Department of Chemistry, Northwestern University, Evanston, IL 60208, USA.

¹²Department of Chemistry, University of Milan, Milan 20133, Italy.

¹³Department of Chemistry, Missouri University of Science and Technology, University of Missouri, Rolla, MO 65409, USA.

* Corresponding author. Email: jrlong@berkeley.edu

† These authors contributed equally to this work.

‡ Present address: Department of Chemistry, Faculty of Science, Mahidol University, Bangkok 10400, Thailand.

§ Present address: Department of Chemistry, Korea Advanced Institute of Science and Technology (KAIST), Daejeon 34141, Republic of Korea.

Abstract: In nature, nonheme iron-containing enzymes use dioxygen to generate high-spin iron(IV)=O species for a variety of oxygenation reactions. Although scientists have long sought to mimic this reactivity, the enzyme-like activation of O₂ to form high-spin iron(IV)=O species remains an unrealized goal in synthetic chemistry. Here, we report a metal–organic framework featuring iron(II) sites with a local structure similar to that in α -ketoglutarate-dependent dioxygenases. The framework reacts with O₂ at low temperatures to form high-spin iron(IV)=O species that are characterized using *in situ* diffuse reflectance infrared Fourier transform, *in situ* and variable-field Mössbauer, Fe K β x-ray emission, and nuclear resonance vibrational spectroscopies. In the presence of O₂, the framework is competent for catalytic oxygenation of cyclohexane and the stoichiometric conversion of ethane to ethanol.

One-Sentence Summary: High-spin Fe(IV)=O species competent for hydrocarbon oxidation are generated using O₂ in a synthetic system that mimics α -ketoglutarate-dependent dioxygenases.

The development of catalysts for the selective oxygenation of light hydrocarbons using O₂ remains a formidable but important challenge in the global effort to develop green technologies for the valorization of natural gas components (1–3). Nature has developed mononuclear nonheme iron metalloenzymes that utilize O₂ for C–H oxygenation chemistry, such as the ubiquitous α -ketoglutarate-dependent dioxygenases (4). One well-studied enzyme in this class is taurine- α -ketoglutarate dioxygenase (TauD), which oxygenates one of the C–H bonds of taurine alpha to the sulfonate group (5). Key to the reactivity of TauD and its family of dioxygenases is a high-spin ($S = 2$) Fe(IV)=O intermediate, which is formed following oxidation of iron(II) with O₂ coupled with oxidation and decarboxylation of the α -ketoglutarate co-substrate (Fig. 1A) (6, 7). Over the last several decades, significant research effort has been devoted to the design and study of iron(IV)-oxo species in molecular (8–17) and iron-zeolite (18, 19) model systems in order to better understand and mimic their reactivity in biological systems. However, most examples studied to date feature an intermediate spin ground state ($S = 1$), and only a small number of these are generated using dioxygen in solution (10–13). High-spin Fe(IV)=O species have been accessed with oxidants such as trimethylammonium-*N*-oxide, hypervalent iodine reagents, and nitrous oxide (14, 15, 18), as well as in the presence of O₂ with light irradiation to cleave the O–O bond (17). However, the use of O₂ alone for the generation of high-spin Fe(IV)=O species, in a manner akin to metalloenzyme reactivity, has yet to be achieved in any synthetic system (16, 19, 20).

Metal-organic frameworks have received increasing attention in recent years as attractive systems for studying biomimetic chemistry (21, 22, 23). These porous, crystalline solids are constructed from metal nodes and organic linkers, and they exhibit chemical and structural tunability that is unmatched in other porous materials (24, 25). As such, metal-organic frameworks offer the opportunity to explore O₂ activation in solid-gas reactions, while the immobilization of metal sites in the lattice may serve to prevent the decomposition of reactive species via dimerization or intramolecular ligand oxidation pathways available to molecular compounds (9, 26, 27). However, reported mimics of nonheme iron enzymes in metal-organic frameworks are scarce (28). In this context, the framework Fe_{1.5}Zn_{3.5}Cl₄(btdd)₃ (H₂btdd = bis(1*H*-1,2,3-triazolo [4,5-*b*],[4',5'-*i*])dibenzo[1,4]dioxin) (29) stands out as a suitable biomimetic platform (22). This material is synthesized via post-synthetic iron(II) exchange in Zn₅Cl₄(btdd)₃ (MFU-4l) (30) and features pseudo-tetrahedral iron(II) sites with tris(triazolate) coordination reminiscent of the binding of the 2-His-1-carboxylate facial triad in TauD. Herein, we report the frameworks Fe_{*x*}Zn_{5-*x*}(prv)₄(btdd)₃ ($x = 1$ or 1.8; Hprv = pyruvic acid) and FeZn₄(moba)₄(btdd)₃ (Hmoba = 3,3-dimethyl-2-oxobutanoic acid), which react with O₂ to generate high-spin ($S = 2$) Fe(IV)=O species that are reactive toward hydrocarbon oxygenation (Figs. 1B and 1C).

Synthesis and characterization of Fe_{*x*}Zn_{5-*x*}(prv)₄(btdd)₃

The frameworks Fe_{*x*}Zn_{5-*x*}(prv)₄(btdd)₃ were prepared via post-synthetic cation exchange in Zn₅Cl₄(btdd)₃ using ferrous chloride and subsequent ligand exchange with pyruvate (see the supplementary materials (SM)). Energy-dispersive x-ray (EDX) spectroscopy revealed that the iron sites in Fe_{*x*}Zn_{5-*x*}Cl₄(btdd)₃ are homogeneously distributed within the materials (figs. S1 and S2), and inductively coupled plasma optical emission spectroscopy (ICP-OES) confirmed the extent of iron substitution. Quantitative exchange of chloride for pyruvate in Fe_{*x*}Zn_{5-*x*}(prv)₄(btdd)₃ is supported by elemental analysis (see section 1.3 of the SM).

Powder x-ray diffraction analysis confirmed that the $\text{Fe}_x\text{Zn}_{5-x}(\text{prv})_4(\text{btdd})_3$ materials are crystalline solids and isostructural to the parent MFU-4l framework (fig. S3), and N_2 adsorption data obtained at 77 K revealed high Brunauer–Emmett–Teller (BET) surface areas of 2130 ± 12 and $2090 \pm 15 \text{ m}^2/\text{g}$ for $x = 1$ and 1.8, respectively (figs. S4 and S5). The 5 K Mössbauer spectrum of desolvated $\text{FeZn}_4(\text{prv})_4(\text{btdd})_3$ features a major doublet (area of 84.2(8)%) with an isomer shift (δ) of 1.061(1) mm/s and a quadrupole splitting ($|\Delta E_Q|$) of 2.567(1) mm/s, indicative of high-spin, five-coordinate iron(II) (fig. S18) (31). Two minor doublets with slightly different Mössbauer parameters likely correspond to six-coordinate iron(II) sites featuring residual coordinating synthesis solvent (table S6). The magnetic circular dichroism spectrum of $\text{FeZn}_4(\text{prv})_4(\text{btdd})_3$ collected at 5 K under a field of 7 T features d-d transitions around 6000 and 14000 cm^{-1} , which are consistent with $S = 2$ iron(II) centers in a five-coordinate ligand field (fig. S8). Continuous-wave parallel mode electron paramagnetic resonance (EPR) spectroscopy and dc magnetic susceptibility data collected for $\text{Fe}_x\text{Zn}_{5-x}(\text{prv})_4(\text{btdd})_3$ further support the assignment of $S = 2$ for the iron(II) sites (figs. S9–S11).

We turned to solid-state ^1H NMR spectroscopy to gain more insight into the possible binding modes of the pyruvate ligands in $\text{FeZn}_4(\text{prv})_4(\text{btdd})_3$, but the broad peaks in the paramagnetic spectrum precluded the extraction of meaningful information (fig. S12). As such, we prepared a crystalline powder sample of $\text{Zn}_5(\text{prv})_4(\text{btdd})_3$ featuring pyruvate labeled with ^{13}C at the methyl carbon. The solid-state ^1H NMR spectrum of $\text{Zn}_5(\text{prv})_4(\text{btdd})_3$ features resonances from the protons of the btdd^{2-} linker and the pyruvate methyl group in approximately a 1:1 ratio, supporting quantitative ligand exchange. We were also able to prepare single crystals of $\text{Zn}_5(\text{prv})_4(\text{btdd})_3$ (see sections 1.6 and 1.7 of the SM and figs. S14A and S15A), and analysis via single-crystal x-ray diffraction revealed that pyruvate coordinates to the peripheral zinc(II) centers in a bidentate fashion (figs. S14B and S15B). It was not possible to isolate single crystals of $\text{FeZn}_4(\text{prv})_4(\text{btdd})_3$ via single-crystal-to-single-crystal exchange starting from $\text{Zn}_5\text{Cl}_4(\text{btdd})_3$. However, the powder x-ray diffraction patterns of $\text{Fe}_x\text{Zn}_{5-x}(\text{prv})_4(\text{btdd})_3$ are consistent with the simulated pattern generated for $\text{Zn}_5(\text{prv})_4(\text{btdd})_3$ from the single-crystal structure (fig. S3), which may indicate that the coordination mode of the pyruvate ligand is similar in the three frameworks.

***In situ* DRIFTS analysis of the reactivity of $\text{Fe}_{1.8}\text{Zn}_{3.2}(\text{prv})_4(\text{btdd})_3$ with O_2**

Reactivity between $\text{Fe}_x\text{Zn}_{5-x}(\text{prv})_4(\text{btdd})_3$ and O_2 was examined with variable-temperature *in situ* diffuse reflectance infrared Fourier transform spectroscopy (DRIFTS) (fig. S16). For this purpose, we used $\text{Fe}_{1.8}\text{Zn}_{3.2}(\text{prv})_4(\text{btdd})_3$ with the goal of maximizing the resulting spectral signal, while $\text{FeZn}_4(\text{prv})_4(\text{btdd})_3$ was used for the remaining spectroscopic analyses described below. Following dosing of a sample of desolvated $\text{Fe}_{1.8}\text{Zn}_{3.2}(\text{prv})_4(\text{btdd})_3$ with O_2 at 100 K, a new absorption band gradually appeared in the DRIFTS spectrum at 2341 cm^{-1} , which we assign as the asymmetric C=O stretch of physisorbed CO_2 formed from decarboxylation of pyruvate (Fig. 2A, solid lines). The intensity of this band increased as the temperature was increased to 150 and 200 K, and above 250 K the band disappeared, consistent with CO_2 desorption from the framework. To verify that the detected CO_2 derived from pyruvate and not from O_2 , we carried out an analogous *in situ* experiment using $\text{Fe}_{1.8}\text{Zn}_{3.2}(1-^{13}\text{C}\text{-prv})_4(\text{btdd})_3$ ($1-^{13}\text{C}\text{-prv}^-$ = pyruvate labeled with ^{13}C on the carboxylate carbon atom) and $^{18}\text{O}_2$ (Fig. 2A, dashed lines). Upon dosing with $^{18}\text{O}_2$ at 100 K, a new stretch appeared at 2275 cm^{-1} , consistent with formation of the isotopologue $^{13}\text{CO}_2$ and not $^{13}\text{C}^{18}\text{O}_2$, confirming that the oxygen atoms do not originate from dioxygen. The $^{13}\text{CO}_2$ stretch grew in intensity with heating to 200 K and disappeared at higher temperatures. A slight deviation of the experimental CO_2 stretching frequencies reported herein from the values associated with gas-phase CO_2 (2349 and 2284 cm^{-1} for CO_2 and $^{13}\text{CO}_2$, respectively) can be ascribed to adsorption of

the CO₂ within the pores of the framework at low temperatures. Importantly, *in situ* powder x-ray diffraction data collected for FeZn₄(prv)₄(btdd)₃ after dosing with O₂ at 100 K over the course of gradual warming to 298 K revealed that the material remains highly crystalline under these conditions (fig. S24).

5

An absorption band was observed to grow in at 831 cm⁻¹ upon dosing Fe_{1.8}Zn_{3.2}(prv)₄(btdd)₃ with O₂ at 100 K, which we assign as an Fe(IV)=O stretch (Fig. 2B, solid lines). This band increased in intensity with heating up to 200 K before diminishing significantly at 250 K and disappearing at 298 K. When the analogous experiment was performed with ¹⁸O₂, the band shifted to 796 cm⁻¹, consistent with a stretching frequency of 794 cm⁻¹ calculated for Fe(IV)=¹⁸O using a simple harmonic oscillator model (Fig. 2B, dashed lines). For comparison, the Fe(IV)=¹⁶O and Fe(IV)=¹⁸O stretches in TauD-*J* appear at 821 and 787 cm⁻¹, respectively (32). Concomitant with the disappearance of the Fe(IV)=O stretch at 250 K, a new stretch appeared at 3628 cm⁻¹ (fig. S17). We attribute this stretch to an Fe(III)-OH species arising from decomposition of the Fe(IV)=O through hydrogen-atom abstraction, possibly from the methyl group of the newly formed acetate ligand (Fig. 2C). At 298 K, a new stretch is apparent at 3678 cm⁻¹ (fig. S17), which may correspond to a different coordination environment for the Fe(III)-OH species at higher temperatures. When ¹⁸O₂ was used for dosing, a stretch appeared at 3617 cm⁻¹, in excellent agreement with that calculated for Fe(III)-¹⁸OH using a simple harmonic oscillator model (3616 cm⁻¹).

20

Experimental and computational investigation of the Fe(IV)=O spin state

25

30

35

The species formed upon reaction of Fe_xZn_{5-x}(prv)₄(btdd)₃ with dioxygen were further investigated by *in situ* Mössbauer spectroscopy (see section 2.9.1 of the SM). As discussed above, the 5 K Mössbauer spectrum of desolvated FeZn₄(prv)₄(btdd)₃ features a major doublet indicative of high-spin, five-coordinate iron(II) (Fig. 3A, table S6). After dosing with 300 mbar of O₂ at 100 K, this doublet persisted and a new doublet was apparent with $\delta = 0.260(4)$ mm/s and $|\Delta E_Q| = 0.572(8)$ mm/s (16.7(2)% area), which we assign to an Fe(IV)=O species. These parameters are similar to those determined for the *S* = 2 Fe(IV)=O intermediate of TauD ($\delta = 0.31$ mm/s and $\Delta E_Q = -0.88$ mm/s) (6, 7). A detailed comparison with isomer shift and quadrupole splitting values for other reported iron(IV)-oxos reveals that they are more consistent with an *S* = 2 spin state ($\delta_{S=2} = 0.02$ – 0.37 mm/s; $|\Delta E_Q|_{S=2} = 0.23$ – 1.27 mm/s) than an *S* = 1 spin state ($\delta_{S=1} < 0.20$ mm/s; $|\Delta E_Q|_{S=1} = 0.44$ – 2.09 mm/s) (see fig. S40). Density functional theory (DFT) calculations at the B3LYP/def2-TZVP level of theory predict an isomer shift of 0.25 mm/s for an *S* = 2 six-coordinate Fe(IV)=O moiety featuring acetate coordinated in a κ^2 -binding mode, in excellent agreement with the experimental value (tables S6 and S9).

40

45

We considered that a slow oxidation rate at 100 K may be a factor limiting the Fe(IV)=O content in O₂-dosed FeZn₄(prv)₄(btdd)₃. Indeed, the percent area of the Fe(IV)=O doublet could be increased up to a maximum of 20.0(2)% upon further dosing with of O₂ at 125 and 150 K. (Fig. 3A, table S6). However, subsequent dosing at 163 K did not result in an increase in the percent of the Fe(IV)=O doublet (figs. S19 and S22). At these temperatures, it is possible that a greater quantity of Fe(IV)=O species is generated initially but that some of these sites react with the acetate ligand to generate a hydroxylated product and reform high-spin iron(II) sites. Analogous

intramolecular α -C–H hydroxylation is known for α -ketoglutarate dependent dioxygenases (35), and we discuss this possibility further below. Finally, spectra were collected at 5 K after heating the sample at 250 and 298 K without additional O₂ dosing. After warming at 250 K, the area of the Fe(IV)=O doublet was only 9.7(3)% and after warming at 298 K, the Fe(IV)=O doublet was absent, consistent with the decomposition observed in the DRIFTS data (fig. S20). A Mössbauer spectrum collected at 5 K after *ex situ* dosing of FeZn₄(prv)₄(btdd)₃ with O₂ at 163 K revealed a slightly higher Fe(IV)=O content of 32.2(6)% relative to that achieved under *in situ* conditions (section 2.9.2 of the SM, fig. S21), which may be due to the different conditions and the nature of the sample used (loose versus compact powder, respectively). The sample remained crystalline after warming to 298 K (fig. S25), and the porosity of the framework did not change significantly (1980±23 m²/g, fig. S26).

The Mössbauer isomer shift and quadrupole splitting values determined for the Fe(IV)=O species generated in FeZn₄(prv)₄(btdd)₃ are more consistent with an $S = 2$ than an $S = 1$ spin state, although these parameters alone do not enable an unambiguous assignment. To experimentally assign the spin state, we turned to applied magnetic field Mössbauer spectroscopy (6, 17, 36). We expected that the low concentration of the Fe(IV)=O species accessible upon dosing FeZn₄(prv)₄(btdd)₃ with O₂ would limit data resolution. One plausible explanation for the low detected concentration is decomposition of the Fe(IV)=O species via oxygenation of the newly formed acetate ligand (35). Such a side reaction would be precluded if pyruvate were replaced with an α -ketocarboxylate lacking α -C–H bonds. Accordingly, we synthesized FeZn₄(moba)₄(btdd)₃, which features a 3,3-dimethyl-2-oxobutyrate ligand with a *tert*-butyl group alpha to the carbonyl (see section 1.8 of the SM). This material is isostructural to Fe_xZn_{5-x}(prv)₄(btdd)₃ (fig. S27) and exhibits a comparably high BET surface area (fig. S28). *In situ* DRIFTS data collected for FeZn₄(moba)₄(btdd)₃ upon dosing with O₂ at 100 K support Fe(IV)=O formation via decarboxylation of 3,3-dimethyl-2-oxobutyrate (see fig. S29; $\nu(\text{Fe}=\text{O}) = 828 \text{ cm}^{-1}$, $\nu(\text{Fe}=\text{O}) = 794 \text{ cm}^{-1}$), consistent with data discussed above for FeZn₄(prv)₄(btdd)₃.

The zero-field Mössbauer spectrum of FeZn₄(moba)₄(btdd)₃ collected at 5 K features a major doublet assigned to high-spin, five-coordinate iron(II) (fig. S31, table S10). Following a sequence of *in situ* dosing with O₂ at 100 K and heating at 200 K, a new quadrupole doublet was apparent in the 5 K Mössbauer spectrum with $\delta = 0.292(1) \text{ mm/s}$ and $\Delta E_Q = -0.603(1) \text{ mm/s}$ (61.7(1)% area), assigned to the Fe(IV)=O species (fig. S31). This relative area is significantly larger than the maximum relative area of *in situ* O₂-dosed FeZn₄(prv)₄(btdd)₃ (21.1(1)%), supporting our hypothesis that intramolecular ligand oxygenation may be limiting the Fe(IV)=O content. Variable-field Mössbauer spectra were subsequently collected for O₂-dosed FeZn₄(moba)₄(btdd)₃ at 1.7 K under fields of ranging from 0 to 7 T and temperatures from 1.7 to 40 K under a field of 7 T (Fig. 3B and fig. S33; see section 2.12 of the SM for details). Spectra were also collected for FeZn₄(moba)₄(btdd)₃ at temperatures <5 K and fields ranging from 0 to 7 T (fig. S32) to obtain fixed parameters for modeling the residual iron(II) species for the O₂-dosed material (table S12; see section 2.12.2 of the SM for details).

Consistent with the zero-field Mössbauer spectrum collected at 5 K, the zero-field spectrum for O₂-dosed FeZn₄(moba)₄(btdd)₃ collected at 1.7 K could be fit with three subspectra, corresponding to an $S = 2$ iron(II) component, an iron(III) species, and an Fe(IV)=O component (Fig. 3B). The isomer shift of this Fe(IV)=O species is consistent with reported $S = 2$ iron(IV)-oxo species in the literature (fig. S40), however, both $S = 1$ and $S = 2$ models were considered in fitting the variable-field and variable-temperature data. Initial attempts to simultaneously fit the variable-temperature data collected under a 7 T field using this three subspectra model did not fully account for the total spectral intensity. We found that inclusion of a fourth subspectrum,

assigned to an $S = 0$ species, likely arising from antiferromagnetically coupled Fe(IV)=O sites within the same cluster node, affords a good fit to the data (see section 2.12.3 of the SM). While ICP-OES analysis predicts a distribution of one iron site per cluster on average, we cannot exclude a distribution wherein some clusters feature two iron centers per cluster, some feature a single iron center, and other clusters contain zero iron sites.

Simultaneous modeling of the variable-field and variable-temperature spectra was performed via diagonalization of the spin Hamiltonians for the four subspectra to obtain values of the zero-field splitting (D) and hyperfine coupling parameters (A_{xx} , A_{yy} , A_{zz}) for the uncoupled Fe(IV)=O species when assigned as either $S = 2$ or $S = 1$ (see section 2.12.3 of the SM for details of the modeling approach and tables S13–15). While the data could be fit with an $S = 2$ or $S = 1$ model (Fig. 3B and figs. S33–S35), only the results for the $S = 2$ model are chemically reasonable based on a comparison with reported Fe(IV)=O species. The best model for the $S = 2$ Fe(IV)=O species yielded $D = 12.7(6) \text{ cm}^{-1}$ and $A_{\text{iso}} = -16.4 \text{ T}$ (see table S13), parameters that are in excellent agreement with those reported for $S = 2$ Fe(IV)=O species ($D_{S=2} = 4\text{--}14 \text{ cm}^{-1}$, $A_{\text{iso}(S=2)} = -23$ to -16 T) (17, 37). In contrast, the best model for $S = 1$ Fe(IV)=O sites yielded values that are significantly different than those reported previously for $S = 1$ Fe(IV)=O species (see table S14) (37, 38, 39). Furthermore, the signs and relative magnitudes of the spin-dipole contribution A^{SD} to the hyperfine coupling tensor are only consistent with an $S = 2$ spin ground state (see section 2.12.4 of the SM).

Additional experimental support for the $S = 2$ assignment for the Fe(IV)=O species was obtained from Fe K β x-ray emission spectroscopy (XES; see section 2.13 of the SM). Iron K β XES involves the measurement of 3p to 1s emissions, and due to the Fe 3p–3d exchange contributions to the final state, the relative intensities and energies of the K β mainline features—the K β' and K $\beta_{1,3}$ peaks—are diagnostic of the local iron spin state (40–42). High-spin states typically give rise to more intense K β' features and larger separations between the K β' and K $\beta_{1,3}$ peaks than low-spin states (41). The XES spectra for $S = 2$ FeZn₄(moba)₄(btdd)₃ and a sample of the framework dosed *ex situ* with O₂ are given in fig. S39, along with a representative spectrum for a reported molecular compound featuring an $S = 1$ Fe(IV)=O (42). The spectra for pristine and O₂-dosed FeZn₄(moba)₄(btdd)₃ nearly overlay and feature an intense K β' peak, consistent with the dominant presence of $S = 2$ iron sites in both materials. In contrast, there is no clear K β' peak in the $S = 1$ Fe(IV)=O spectrum, and the K $\beta_{1,3}$ peak appears at a lower energy than in the spectrum for O₂-dosed FeZn₄(moba)₄(btdd)₃.

Finally, we used DFT to calculate Mössbauer isomer shifts for the model cluster Fe(O)(κ^2 -OPiv)Zn₄(prv)₃(bta)₆ (OPiv[−] = pivalate formed upon moba[−] decarboxylation; bta[−] = benzotriazolate) featuring an $S = 2$ or $S = 1$ ground state. Geometry optimizations were performed at the BP86-D3BJ/def2-TZVP level of theory. For the $S = 2$ optimized geometry, $\delta_{\text{calc}} = 0.27 \text{ mm/s}$ is in excellent agreement with the experimentally determined isomer shift ($\delta = 0.292(1) \text{ mm/s}$), whereas the isomer shift calculated for $S = 1$ deviates significantly from the experimental value ($\delta_{\text{calc}} = 0.16 \text{ mm/s}$) (table S11). Furthermore, CASSCF calculations in combination with N -electron valence perturbation theory to second order (NEVPT2) support the assignment of an $S = 2$ ground state, which is predicted to be 25 kcal/mol more stable than the lowest energy $S = 1$ configuration (see section 3 of the SM and fig. S41). Altogether, the Mössbauer, Fe K β XES, and computational data clearly support the assignment of an $S = 2$ ground state for the Fe(IV)=O sites formed upon oxidation of FeZn₄(moba)₄(btdd)₃.

Investigation of the local Fe(IV)=O coordination environment using nuclear resonance vibrational spectroscopy

Nuclear resonance vibrational spectroscopy (NRVS) was used to gain further insight into the local structure of the Fe(IV)=O species (see section 2.7 of the SM). This technique selectively yields the complete set of vibrational modes of Mössbauer-active nuclei and can therefore provide structural insights not accessible using other spectroscopic methods. Figures 4A and B, respectively, show the iron partial vibrational density of states (PVDOS) distributions obtained from data collected at ~100 K for desolvated 95% ⁵⁷Fe-enriched FeZn₄(prv)₄(btdd)₃ before and after *ex situ* O₂-dosing at 163 K. A new peak at 822 cm⁻¹ for the O₂-dosed sample was assigned to an Fe(IV)=O vibration and is similar in magnitude to NRVS peaks reported for other nonheme Fe(IV)=O species in synthetic systems (33, 43, 44). In support of this assignment, when ¹⁸O₂ was employed for dosing, the vibration appeared instead at 788 cm⁻¹ (Fig. 4B, inset; figs. S44 and S47). Consistent results were obtained from PVDOS distributions obtained for ⁵⁷Fe-enriched FeZn₄(moba)₄(btdd)₃ after dosing with O₂ or ¹⁸O₂ (fig. S50), which feature peaks at 820 and 789 cm⁻¹, respectively. The Fe(IV)=O peak was absent in the PVDOS distribution obtained for both frameworks after warming to 298 K (figs. S43 and S51).

Using the truncated cluster FeZn₄(prv)₄(bta)₆ as a model for FeZn₄(prv)₄(btdd)₃, we performed DFT calculations to simulate the NRVS iron PVDOS for the framework before and after O₂ dosing (Figs. 4A and 4B, dark gray curves). The intense stretch at 330 cm⁻¹ predicted for the model iron(II) framework corresponds to vibrations associated with bidentate pyruvate binding. Differences in the predicted and experimental intensities likely arise because the cluster model cannot fully describe the phonons of the framework lattice. For the O₂-dosed sample, stretches at 282 and 340 cm⁻¹ are assigned as Fe–O vibrations resulting from κ²-binding of the acetate ligand (Fig. 4C). In contrast, Fe–O vibrations associated with κ¹-binding of acetate are predicted to appear at higher wavenumbers (>400 cm⁻¹) (figs. S45 and S46). The calculated Fe(IV)=O stretch is higher than the experimental stretching frequency (919 versus 822 cm⁻¹), likely because of a known systematic overestimation by DFT at these higher energies, which is less pronounced at lower energies (45). Finally, simulated NRVS iron PVDOS were also generated for pristine and O₂-dosed FeZn₄(moba)₄(btdd)₃ from DFT calculations on the truncated *S* = 2 cluster models Fe(moba)Zn₄(prv)₃(bta)₆ and Fe(O)(κ²-OPiv)Zn₄(prv)₃(bta)₆, and the results are in good agreement with the experiment (figs. S48 and S49).

Reactivity studies

We evaluated the reactivity of Fe_{*x*}Zn_{5-*x*}(prv)₄(btdd)₃ with hydrocarbon substrates in the presence of O₂. Desolvated FeZn₄(prv)₄(btdd)₃ was suspended in cyclohexane and exposed to 1 bar of O₂ at 21 °C for 24 h. Subsequently, CH₃CN-*d*₃ was added to extract the products, along with CH₂Br₂ as an internal standard. Analysis of the resulting supernatant using ¹H NMR spectroscopy and GC-MS revealed the formation of cyclohexanol (22% NMR yield with respect to the iron sites in the framework) with no detectable cyclohexanone (see section 1.9.1 of the SM and figs. S53 and S54). Mössbauer spectroscopy analysis of the framework isolated following this reaction revealed only iron(II) species (fig. S56). The same stoichiometric reaction was also carried out using FeZn₄(moba)₄(btdd)₃ in the presence of O₂ (1 bar, 21 °C), and analysis of the resulting supernatant using ¹H NMR spectroscopy and GC-MS revealed the formation of only cyclohexanol (51% NMR yield) (see section 1.11.1 of the SM and figs. S59 and S60). A stoichiometric control reaction between cyclohexane and FeZn₄Cl₄(btdd)₃ in the presence of O₂ did not yield any hydrocarbon oxidation products (figs. S57 and S58).

In order to establish the direct role of the Fe(IV)=O species in C–H oxygenation, we sought to perform a stoichiometric reaction using a framework sample in which the Fe(IV)=O species were

generated prior to the addition of substrate. A sample of $\text{FeZn}_4(\text{prv})_4(\text{btdd})_3$ was dosed with 200 mbar O_2 at 163 K, and after 2 h, the sample headspace was evacuated, refilled with Ar and a mixture of cyclohexane and CD_2Cl_2 was added. The suspension was then warmed to 195 K and held for 2 h and then allowed to warm to 294 K. Under these conditions, no cyclohexane oxidation products were detected via ^1H NMR spectroscopy. When a similar reaction was performed using $\text{FeZn}_4(\text{moba})_4(\text{btdd})_3$ (see section 1.11.2 of the SM), ^1H NMR spectroscopy and GC-MS analysis of the resulting supernatant revealed the formation of cyclohexanone (figs. S61 and S62; 48% NMR yield). The ultimate formation of cyclohexanone in this case—in contrast to cyclohexanol formed in the reaction conducted at 21 °C—is attributed to the lower reaction temperature and slower diffusion of cyclohexanol out of the framework pores, which is then further oxidized to cyclohexanone (see section 1.11 of the SM) (46).

When the cyclohexane oxidation reaction with $\text{FeZn}_4(\text{prv})_4(\text{btdd})_3$ was repeated with the addition of 11 equivalents of pyruvic acid, cyclohexanone and cyclohexanol were obtained in a 2:1 ratio (combined yield of 173%) (see section 1.9.2 of the SM and fig. S64). Powder x-ray diffraction analysis of the solid isolated from this reaction confirmed that the framework remains crystalline (fig. S65). Significantly, this result suggests that $\text{FeZn}_4(\text{prv})_4(\text{btdd})_3$ can act as a catalyst in hydrocarbon oxidation reactions using the free α -keto acid as a co-substrate, presumably via a similar catalytic cycle as proposed for TauD (fig. S71) (6). We found that acetic acid byproduct is formed in this reaction in 288% yield with respect to the iron sites, which suggests 115% of pyruvic acid conversion to unidentified products. Such unproductive turnover at some of the iron sites is consistent with the relatively low yield in the stoichiometric reaction. A number of studies of synthetic and enzymatic systems have established that C–H bond activation by $\text{Fe}(\text{IV})=\text{O}$ species proceeds via H-atom abstraction, as evidenced by large primary kinetic isotope effects (KIEs) (46, 47). Consistent with these results, we determined an intermolecular competition KIE value of 29.8 ± 1.0 from the reaction of $\text{FeZn}_4(\text{prv})_4(\text{btdd})_3$ with a mixture of cyclohexane and cyclohexane- d_{12} under an atmosphere of O_2 (see section 1.10 of the SM and figs. S66 and S67).

The reactivity of $\text{Fe}_{1.8}\text{Zn}_{3.2}(\text{prv})_4(\text{btdd})_3$ in the presence of O_2 was also evaluated using gaseous ethane as a substrate in a high-pressure batch reactor (section 1.12 of the SM). Using a high-pressure mixture of ethane and dioxygen, ethanol and acetaldehyde were obtained in a 3:1 ratio with a high combined yield of 82% (fig. S68). This yield is much higher than that obtained in the stoichiometric cyclohexane oxidation, likely due to the high ethane concentration close to the iron sites under high pressure. Although there are enzymatic systems capable of oxidizing ethane to ethanol with O_2 (48), our result is the first synthetic example of ethane oxidation via an unambiguously characterized $S = 2$ $\text{Fe}(\text{IV})=\text{O}$ intermediate generated by O_2 .

Outlook

We have developed the frameworks $\text{Fe}_x\text{Zn}_{5-x}(\text{prv})_4(\text{btdd})_3$ and $\text{FeZn}_4(\text{moba})_4(\text{btdd})_3$ featuring iron(II) sites that activate O_2 at 100 K to form high-spin $\text{Fe}(\text{IV})=\text{O}$ species; reactivity that is reminiscent of O_2 activation in TauD. These frameworks are rare non-enzymatic systems capable of catalytic hydrocarbon oxygenation, including the oxidation of ethane to ethanol, via a reactive high-spin $\text{Fe}(\text{IV})=\text{O}$ intermediate generated from dioxygen. This work establishes a foundation for the development of iron-containing metal–organic frameworks as heterogenous catalysts that closely mimic the reactivity of metalloenzymes.

References and Notes

1. B. G. Hashiguchi, M. M. Konnick, S. M. Bischof, S. J. Gustafson, D. Devarajan, N.

- Gunsalus, D. H. Ess, R. A. Periana, Main-group compounds selectively oxidize mixtures of methane, ethane, and propane to alcohol esters. *Science* **343**, 1232–1237 (2014).
2. J. Shan, M. Li, L. F. Allard, S. Lee, M. Flytzani-Stephanopoulos, Mild oxidation of methane to methanol or acetic acid on supported isolated rhodium catalysts. *Nature* **551**, 605–608 (2017).
- 5 3. V. L. Sushkevich, D. Palagin, M. Ranocchiari, J. A. van Bokhoven, Selective anaerobic oxidation of methane enables direct synthesis of methanol. *Science* **356**, 523–527 (2017).
4. E. G. Kovaleva, J. D. Lipscomb, Versatility of biological non-heme Fe(II) centers in oxygen activation reactions. *Nat. Chem. Biol.* **4**, 186–193 (2008).
- 10 5. C. Krebs, D. G. Fujimori, C. T. Walsh, J. M. Bollinger Jr., Non-heme Fe(IV)–oxo intermediates. *Acc. Chem. Res.* **40**, 484–492 (2007).
6. J. C. Price, E. W. Barr, B. Tirupati, J. M. Bollinger Jr., C. Krebs, The first direct characterization of a high-valent iron intermediate in the reaction of an α -ketoglutarate-dependent dioxygenase: a high-spin Fe(IV) complex in taurine/ α -ketoglutarate dioxygenase (TauD) from *Escherichia coli*. *Biochemistry*. **42**, 7497–7508 (2003).
- 15 7. S. Sinnecker, N. Svensen, E. W. Barr, S. Ye, J. M. Bollinger Jr., F. Neese, C. Krebs, Spectroscopic and computational evaluation of the structure of the high-spin Fe(IV)-oxo intermediates in taurine: α -ketoglutarate dioxygenase from *Escherichia coli* and its His99Ala ligand variant. *J. Am. Chem. Soc.* **129**, 6168–6179 (2007).
- 20 8. J. Hohenberger, K. Ray, K. Meyer, The biology and chemistry of high-valent iron–oxo and iron–nitrido complexes. *Nat. Commun.* **3**, 1–13 (2012).
9. M. P. Mehn, K. Fujisawa, E. L. Hegg, L. Que Jr., Oxygen activation by nonheme iron(II) complexes: α -keto carboxylate versus carboxylate. *J. Am. Chem. Soc.* **125**, 7828–7842 (2003).
- 25 10. A. Thibon, J. England, M. Martinho, V. G. Young Jr., J. R. Frisch, R. Guillot, J. J. Girerd, E. Münck, L. Que Jr., F. Banse, Proton- and reductant-assisted dioxygen activation by a nonheme iron(II) complex to form an oxoiron(IV) intermediate. *Angew. Chem. Int. Ed.* **47**, 7064–7067 (2008).
- 30 11. F. Li, K. M. Van Heuvelen, K. K. Meier, E. Münck, L. Que Jr., Sc^{3+} -triggered oxoiron(IV) formation from O_2 and its non-heme iron(II) precursor via a Sc^{3+} -peroxo- Fe^{3+} intermediate, *J. Am. Chem. Soc.* **135**, 28, 10198–10201 (2013).
12. D. Kass, T. Corona, K. Warm, B. Braun-Cula, U. Kuhlmann, E. Bill, S. Mebs, M. Swart, H. Dau, M. Haumann, P. Hildebrandt, K. Ray, Stoichiometric formation of an oxoiron(IV) complex by a soluble methane monooxygenase type activation of O_2 at an iron(II)-cyclam center, *J. Am. Chem. Soc.* **142**, 13, 5924–5928 (2020).
- 35 13. M. A. Dedushko, M. B. Greiner, A. N. Downing, M. Coggins, J. A. Kovacs, Electronic structure and reactivity of dioxygen-derived aliphatic thiolate-ligated Fe-peroxo and Fe(IV) oxo compounds. *J. Am. Chem. Soc.* **144**, 8515–8528 (2022).
- 40 14. J. P. Bigi, W. H. Harman, B. Lassalle-Kaiser, D. M. Robles, T. A. Stich, J. Yano, R. D. Britt, C. J. Chang, A high-spin iron(IV)-oxo complex supported by a trigonal nonheme pyrrolide platform. *J. Am. Chem. Soc.* **134**, 1536–1542 (2012).

15. M. Puri, L. Que Jr., Toward the synthesis of more reactive $S = 2$ non-heme oxoiron(IV) complexes. *Acc. Chem. Res.* **48**, 2443–2452 (2015).
16. C. E. MacBeth, A. P. Golombek, J. Victor G. Young, C. Yang, K. Kuczera, M. P. Hendrich, A. S. Borovik, O_2 activation by nonheme iron complexes: a monomeric Fe(III)-oxo complex derived from O_2 . *Science* **289**, 938–941 (2000).
17. J. B. Gordon, T. Albert, A. Dey, S. Sabuncu, M. A. Siegler, E. Bill, P. Moënné-Loccoz, D. P. Goldberg, A reactive, photogenerated high-spin ($S = 2$) $Fe^{IV}(O)$ complex via O_2 activation. *J. Am. Chem. Soc.* **143**, 21637–21647 (2021).
18. B. E. R. Snyder, P. Vanelderen, M. L. Bols, S. D. Hallaert, L. H. Böttger, L. Ungur, K. Pierloot, R. A. Schoonheydt, B. F. Sels, E. I. Solomon, The active site of low-temperature methane hydroxylation in iron-containing zeolites. *Nature* **536**, 317–321 (2016).
19. E. Tabor, J. Dedecek, K. Mlekodaj, Z. Sobalik, P. C. Andrikopoulos, S. Sklenak, Dioxygen dissociation over man-made system at room temperature to form the active α -oxygen for methane oxidation. *Sci. Adv.* **6**, eaaz9776 (2020).
20. B. Rungtaweevoranit, A. M. Abdel-Mageed, P. Khemthong, S. Eaimsumang, K. Chakarawet, T. Butburee, B. Kunkel, S. Wohlrab, K. Chainok, J. Phanthasri, S. Wannapaiboon, S. Youngjan, T. Seehamongkol, S. Impeng, K. Faungnawakij, Structural evolution of iron-loaded metal–organic framework catalysts for continuous gas-phase oxidation of methane to methanol. *ACS Appl. Mater. Interfaces* **15**, 26700–26709 (2023).
21. A. M. Wright, Z. Wu, G. Zhang, J. L. Mancuso, R. J. Comito, R. W. Day, C. H. Hendon, J. T. Miller, M. Dincă, A structural mimic of carbonic anhydrase in a metal-organic framework. *Chem.* **4**, 2894–2901 (2018).
22. C. E. Bien, K. K. Chen, S.-C. Chien, B. R. Reiner, L.-C. Lin, C. R. Wade, W. S. W. Ho, Bioinspired metal–organic framework for trace CO_2 capture. *J. Am. Chem. Soc.* **140**, 12662–12666 (2018).
23. J. G. Vitillo, C. C. Lu, A. Bhan, L. Gagliardi, Comparing the reaction profiles of single iron catalytic sites in enzymes and in reticular frameworks for methane-to-methanol oxidation. *Cell Rep. Phys. Sci.*, **4**, 101422 (2023).
24. H.-C. Zhou, J. R. Long, O. M. Yaghi, Introduction to metal–organic frameworks. *Chem. Rev.* **112**, 673–674 (2012).
25. H. Furukawa, K. E. Cordova, M. O’Keeffe, O. M. Yaghi, The chemistry and applications of metal–organic frameworks. *Science* **341**, 1230444 (2013).
26. D. J. Xiao, E. D. Bloch, J. A. Mason, W. L. Queen, M. R. Hudson, N. Planas, J. Borycz, A. L. Dzubak, P. Verma, K. Lee, F. Bonino, V. Crocellà, J. Yano, S. Bordiga, D. G. Truhlar, L. Gagliardi, C. M. Brown, J. R. Long, Oxidation of ethane to ethanol by N_2O in a metal–organic framework with coordinatively unsaturated iron(II) sites. *Nat. Chem.* **6**, 590–595 (2014).
27. A. Illiescu, J. J. Oppenheim, C. Sun, M. Dincă, Conceptual and practical aspects of metal–organic frameworks for solid–gas reactions. *Chem. Rev.* **123**, 6197–6232 (2023).
28. A. Shaabani, R. Mohammadian, H. Farhid, M. K. Alavijeh, M. M. Amini, Iron-decorated, guanidine functionalized metal–organic framework as a non-heme iron-based enzyme mimic system for catalytic oxidation of organic substrates. *Catal. Lett.* **149**, 1237–1249

(2019).

29. D. Denysenko, J. Jelic, K. Reuter, D. Volkmer, Postsynthetic metal and ligand exchange in MFU-4l: a screening approach toward functional metal–organic frameworks comprising single-site active centers. *Chem. Eur. J.* **21**, 8188–8199 (2015).
- 5 30. D. Denysenko, M. Grzywa, M. Tonigold, B. Streppel, I. Krkljus, M. Hirscher, E. Mugnaioli, U. Kolb, J. Hanss, D. Volkmer, Elucidating gating effects for hydrogen sorption in MFU-4-type triazolate-based metal–organic frameworks featuring different pore sizes. *Chem. Eur. J.* **17**, 1837–1848 (2011).
- 10 31. P. Gütllich, E. Bill, A. X. Trautwein, *Mössbauer Spectroscopy and Transition Metal Chemistry* (Springer-Verlag, Berlin-Heidelberg, Germany, 2011).
32. D. A. Proshlyakov, T. F. Henshaw, G. R. Monterosso, M. J. Ryle, R. P. Hausinger, Direct detection of oxygen intermediates in the non-heme Fe enzyme taurine/ α -ketoglutarate dioxygenase. *J. Am. Chem. Soc.* **126**, 1022–1023 (2004).
- 15 33. V. F. Oswald, J. L. Lee, S. Biswas, A. C. Weitz, K. Mittra, R. Fan, J. Li, J. Zhao, M. Y. Hu, E. E. Alp, E. L. Bominaar, Y. Guo, M. T. Green, M. P. Hendrich, A. S. Borovik, Effects of noncovalent interactions on high-spin Fe(IV)–oxido complexes. *J. Am. Chem. Soc.* **142**, 11804–11817 (2020).
- 20 34. K. Warm, A. Paskin, U. Kuhlmann, E. Bill, M. Swart, M. Haumann, H. Dau, P. Hildebrandt, K. Ray, A pseudotetrahedral terminal oxoiron(IV) complex: mechanistic promiscuity in C–H Bond oxidation reactions. *Angew. Chem. Int. Ed.* **60**, 6752–6756 (2021).
- 25 35. M. G. Thompson, J. M. Blake-Hedges, J. H. Pereira, J. A. Hangasky, M. S. Belcher, W. M. Moore, J. F. Barajas, P. Cruz-Morales, L. J. Washington, R. W. Haushalter, C. B. Eiben, Y. Liu, W. Skyrud, V. T. Benites, T. P. Barnum, E. E. K. Baidoo, H. V. Scheller, M. A. Marletta, P. M. Shih, P. D. Adams, J. D. Keasling, An iron (II) dependent oxygenase performs the last missing step of plant lysine catabolism. *Nat. Commun.* **11**, 2931 (2020).
36. V. Ksenofontov, H. Spiering, S. Reiman, Y. Garcia, A. B. Gaspar, J. A. Real, P. Gütllich, Determination of spin state in dinuclear iron(II) coordination compounds using applied field Mössbauer spectroscopy. *Hyperfine Interact.* **141**, 47–52 (2002).
- 30 37. A. R. McDonald, L. Que Jr., High-valent nonheme iron-oxo complexes: synthesis, structure, and spectroscopy. *Coord. Chem. Rev.* **257**, 414–428 (2013).
38. T. A. Jackson, J.-U. Rohde, M. S. Seo, C. V. Sastri, R. DeHont, A. Stubna, T. Ohta, T. Kitagawa, E. Münck, W. Nam, L. Que Jr., Axial ligand effects on the geometric and electronic structures of nonheme oxoiron(IV) complexes. *J. Am. Chem. Soc.* **130**, 12394–12407 (2008).
- 35 39. J. England, M. Martinho, E. R. Farquhar, J. R. Frisch, E. L. Bominaar, E. Münck, L. Que Jr., A synthetic high-spin oxoiron(IV) complex: generation, spectroscopic characterization, and reactivity. *Angew. Chem., Int. Ed.* **48**, 3622–3626 (2009).
- 40 40. N. Lee, T. Petrenko, U. Bergmann, F. Neese, S. DeBeer, Probing valence orbital composition with iron $K\beta$ x-ray emission spectroscopy. *J. Am. Chem. Soc.* **132**, 9715–9727 (2010).

41. C. J. Pollock, M. U. Delgado-Jaime, M. Atanasov, F. Neese, S. DeBeer, K β mainline x-ray emission spectroscopy as an experimental probe of metal–ligand covalency. *J. Am. Chem. Soc.* **136**, 9453–9463 (2014).
42. G. E. Cutsail III, R. Banerjee, D. B. Rice, O. McCubbin Stepanic, J. D. Lipscomb, S. DeBeer, Determination of the iron(IV) local spin states of the Q intermediate of soluble methane monooxygenase by K β x-ray emission spectroscopy. *J. Biol. Inorg. Chem.* **27**, 573–582 (2022).
43. C. B. Bell, S. D. Wong, Y. Xiao, E. J. Klinker, A. L. Tenderholt, M. C. Smith, J.-U. Rohde, L. Que Jr., S. P. Cramer, E. I. Solomon, A combined NRVS and DFT study of Fe^{IV}-O model complexes: a diagnostic method for the elucidation of non-heme iron enzyme intermediates. *Angew. Chem. Int. Ed.* **47**, 9071–9074 (2008).
44. A. C. Weitz, E. A. Hill, V. F. Oswald, E. L. Bominaar, A. S. Borovik, M. P. Hendrich, Y. Guo, Probing hydrogen bonding interactions to iron-oxido/hydroxido units by ⁵⁷Fe nuclear resonance vibrational spectroscopy. *Angew. Chem. Int. Ed.* **57**, 16010–16014 (2018).
45. B. E. R. Snyder, L. H. Böttger, M. L. Bols, J. J. Yan, H. M. Rhoda, A. B. Jacobs, M. Y. Hu, J. Zhao, E. E. Alp, B. Hedman, K. O. Hodgson, R. A. Schoonheydt, B. F. Sels, E. I. Solomon, Structural characterization of a non-heme iron active site in zeolites that hydroxylates methane. *Proc. Natl. Acad. Sci. U. S. A.* **115**, 4565–4570 (2018).
46. A. N. Biswas, M. Puri, K. K. Meier, W. N. Oloo, G. T. Rohde, E. L. Bominaar, E. Münck, L. Que Jr., Modeling TauD-J: A high-spin nonheme oxoiron(IV) complex with high reactivity toward C–H bonds. *J. Am. Chem. Soc.* **137**, 2428–2431 (2015).
47. J. C. Price, E. W. Barr, T. E. Glass, C. Krebs, J. M. Bollinger Jr., Evidence for hydrogen abstraction from C1 of taurine by the high-spin Fe(IV) intermediate detected during oxygen activation by taurine: α -ketoglutarate dioxygenase (TauD). *J. Am. Chem. Soc.* **125**, 13008–13009 (2003).
48. P. Meinhold, M. W. Peters, M. M. Y. Chen, K. Takahashi, F. H. Arnold, Direct conversion of ethane to ethanol by engineered cytochrome P450 BM3. *ChemBioChem* **6**, 1765–1768 (2005).
49. S. O. Nwaukwa, P. M. Keehn, The oxidation of alcohols and ethers using calcium hypochlorite [Ca(OCl)₂], *Tetrahedron Lett*, **23**, 35 (1982).
50. G. M. Sheldrick, SHELXT – Integrated space-group and crystal-structure determination. *Acta Crystallogr. A*, **71**, 3–8 (2015).
51. G. M. Sheldrick, SHELXT and SHELXL, University of Göttingen, Germany (2015).
52. O. V. Dolomanov, L. J. Bourhis, R. J. Gildea, J. A. K. Howard, H. Puschmann, OLEX2: a complete structure solution, refinement and analysis program. *J. Appl. Crystallogr.* **42**, 339–341 (2009).
53. A. L. Spek, PLATON SQUEEZE: a tool for the calculation of the disordered solvent contribution to the calculated structure factors. *Acta Crystallogr. C*, **71**, 9 (2015).
54. S. Stoll, A. Schweiger, EasySpin, a comprehensive software package for spectral simulation and analysis in EPR. *J. Magn. Reson.* **178**, 42–55 (2006).

55. W. Sturhahn, CONUSS and PHOENIX: Evaluation of nuclear resonant scattering data. *Hyperfine Interact.* **125**,149–172 (2000).
56. W. Sturhahn, T. S. Toellner, E. E. Alp, X. Zhang, M. Ando, Y. Yoda, S. Kikuta, M. Seto, C. W. Kimball, B. Dabrowski, Phonon density of states measured by inelastic nuclear resonant scattering. *Phys. Rev. Lett.* **74**, 3832–3835 (1995).
57. Gnuplot 5.2, An Interactive Plotting Program, Thomas Williams & Colin Kelley, (2019).
58. C. K. Brozek, A. Ozarowski, S. A. Stoian, M. Dincă, Dynamic structural flexibility of Fe-MOF-5 rvidenced by ^{57}Fe Mössbauer spectroscopy. *Inorg. Chem. Front.* **4**, 782–788 (2017).
59. C. Gallenkamp, U. Kramm, J. Proppe, V. Krewald, Calibration of computational Mössbauer spectroscopy to unravel active sites in FeNC catalysts for the oxygen reduction reaction. *Int. J. Quantum Chem.* **121**, e26394 (2021).
60. E. Koch, Exchange Mechanisms. in *Correlated electrons: From models to materials*, Forschungszentrum Jülich GmbH Institute for Advanced Simulation (2012).
61. J. B. Goodenough, Theory of the role of covalence in the perovskite-type manganites [La, M(II)]MnO₃. *Phys. Rev.* **100**, 564–573 (1955).
62. J. B. Goodenough, An interpretation of the magnetic properties of the perovskite-type mixed crystals La_{1-x}Sr_xCoO_{3-λ}. *J. Phys. Chem. Solids* **6**, 287–297 (1958).
63. J. Kanamori, Superexchange interaction and symmetry properties of electron orbitals. *J. Phys. Chem. Solids* **10**, 87–98 (1959).
64. F. Lloret, M. Julve, J. Cano, G. De Munno, Topology and spin polarization in sheetlike metal(II) polymers: ML₂X₂ (M = Mn, Fe, Co or Ni, L = pyrimidine or pyrazine and X = NCS or NCO). *Mol. Cryst. Liquid Cryst. Science Tech. A* **334**, 569–585 (1999).
65. F. Biaso, C. Duboc, B. Barbara, G. Serratrice, F. Thomas, D. Charapoff; C. Béguin, High-field EPR study of frozen aqueous solutions of iron(III) citrate complexes. *Eur. J. Inorg. Chem.*, 467–478 (2005).
66. J. Telsler, EPR interactions – zero-field splittings. *eMagRes* **6**, 207–234 (2017).
67. C. E. Schulz, R. Rutter, J. T. Sage, P. G. Debrunner, Mössbauer and electron paramagnetic resonance studies of horseradish peroxidase and its catalytic iintermediates. *Biochemistry* **23**, 4743–4754 (1984).
68. G. A. Grapperhaus, B. Mienert, E. Bill, T. Weyhermüller, K. Wieghardt, Mononuclear (nitrido)iron(V) and (oxo)iron(IV) complexes via photolysis of [(cyclam-acetato)Fe^{III}(N₃)]⁺ and ozonolysis of [(cyclam-acetato)Fe^{III}(O₃SCF₃)]⁺ in water/acetone mixtures. *Inorg. Chem.* **39**, 5306–5317 (2000).
69. J. F. Berry, E. Bill, E. Bothe, F. Neese, K. Wieghardt, Octahedral non-heme oxo and non-oxo Fe(IV) complexes: an experimental/theoretical comparison. *J. Am. Chem. Soc.* **128**, 13515–13528 (2006).
70. M. Bennati, "EPR Interactions – Hyperfine Couplings." in *EPR Spectroscopy: Fundamentals and Methods*, D. Goldfarb, S. Stoll, Eds. (John Wiley & Sons, 2018), pp. 81–94.

71. N. M. Atherton, "The anisotropic hyperfine interaction." in *Principles of Electron Spin Resonance*, (Ellis Horwood, 1993), pp. 169–223.
72. G. Hölzer, M. Fritsch, M. Deutsch, J. Härtwig, E. Förster, $K\alpha_{1,2}$ and $K\beta_{1,3}$ x-ray emission lines of the 3d transition metals. *Phys. Rev. A* **56**, 4554–4568 (1997).
- 5 73. F. Neese, The ORCA program system. *Wiley Interdiscip. Rev. Comput. Mol. Sci.* **2**, 73–78 (2012).
74. A. D. Becke, Density-functional thermochemistry. III. The role of exact exchange, *J. Chem. Phys.* **98**, 5648–5652(1993).
- 10 75. C. Lee, W. Yang, R. G. Parr, Development of the Colle-Salvetti correlation-energy formula into a functional of the electron density. *Phys. Rev. B* **37**, 785–789 (1988).
76. F. Weigend, R. Ahlrichs, Balanced basis sets of split valence, triple zeta valence and quadruple zeta valence quality for H to Rn: design and assessment of accuracy, *Phys. Chem. Chem. Phys.* **7**, 3297–3305 (2005).
- 15 77. A. D. Becke, Density-functional exchange-energy approximation with correct asymptotic behavior. *Phys. Rev. A* **38**, 3098–3100 (1988).
78. S. Grimme, S. Ehrlich, L. Goerigk, Effect of the damping function in dispersion corrected density functional theory. *J. Comput. Chem.* **32**, 1456–1465 (2011).
79. F. Neese, Prediction and interpretation of the ^{57}Fe isomer shift in Mössbauer spectra by density functional theory. *Inorg. Chim. Acta* **337**, 181-192 (2002).
- 20 80. M. Römelt, S. Ye, F. Neese, Calibration of modern density functional theory methods for the prediction of ^{57}Fe Mössbauer isomer shifts: meta-GGA and double-hybrid functionals. *Inorg. Chem.* **48**, 784–785 (2009).
81. P.-Å. Malmqvist, B. O. Roos, The CASSCF state interaction method. *Chem. Phys. Lett.* **155**, 189–194 (1989).
- 25 82. C. Angeli, R. Cimiraglia, J.-P. Malrieu, N-electron valence state perturbation theory: A spinless formulation and an efficient implementation of the strongly contracted and of the partially contracted variants. *J. Chem. Phys.* **117**, 9138–9153 (2002).
83. F. Neese, Definition of corresponding orbitals and the diradical character in broken symmetry DFT calculations on spin coupled systems. *J. Phys. Chem. Solids* **65**, 781–785 (2004).
- 30 84. G. A. Zhurko, Chemcraft - graphical program for visualization of quantum chemistry computations. <https://chemcraftprog.com>.
85. Diamond-Crystal and Molecular Structure Visualization, Crystal Impact. <https://www.crystalimpact.de/diamond>.
- 35 86. G. Le Caër, J. M. Dubois, Evaluation of hyperfine parameter distributions from overlapped Mössbauer spectra of amorphous alloys. *J. Phys. E: Sci. Instrum.* **12**, 1083–1090 (1979).
- 40 87. J.-U. Rohde, J.-H. In, M. H. Lim, W. W. Brennessel, M R. Bukowski, A. Stubna, E. Münck, W. Nam, L. Que Jr., Crystallographic and spectroscopic evidence for a nonheme Fe(IV)=O complex. *Science* **299**, 1037–1039 (2003).

88. J. Kaizer, E. J. Klinker, N. Y. Oh, J.-U. Rohde, W. J. Song, A. Stubna, J. Kim, E. Münck, W. Nam, L. Que Jr., Nonheme Fe^{IV}O complexes that can oxidize the C–H bonds of cyclohexane at Room Temperature. *J. Am. Chem. Soc.* **126**, 472–473 (2004).
89. O. Pestovsky, S. Stoian, E. L. Bominaar, X. Shan, E. Münck, L. Que Jr.; A. Bakac, Aqueous Fe^{IV}=O: spectroscopic identification and oxo group exchange. *Angew. Chem. Int. Ed.* **44**, 6871–6874 (2005).
90. J. England, Y. Guo, K. M. Van Heuvelen, M. A. Cranswick, G. T. Rohde, E. L. Bominaar, E. Münck, L. Que Jr., A more reactive trigonal bipyramidal high-spin oxoiron(IV) complex with a cis-labile site. *J. Am. Chem. Soc.* **133**, 11880–11883 (2011).
91. D. C. Lacy, R. Gupta, K. L. Stone, J. Greaves, J. W. Ziller, M. P. Hendrich, A. S. Borovik, Formation, structure, and EPR detection of a high spin Fe^{IV}–oxo species derived from either an Fe^{III}–Oxo or Fe^{III}–OH Complex. *J. Am. Chem. Soc.* **132**, 12188–12190 (2010).
92. G. Xue, A. T. Fiedler, M. Martinho, E. Münck, L. Que Jr., Insights into the P-to-Q conversion in the catalytic cycle of methane monooxygenase from a synthetic model system. *Proc. Natl. Acad. Sci. U. S. A.* **105**, 20615–20620 (2008).
93. G. Xue, D. Wang, R. De Hont, A. T. Fiedler, X. Shan, E. Münck, L. Que Jr., A synthetic precedent for the [Fe^{IV}₂(μ-O)₂] diamond core proposed for methane monooxygenase intermediate Q. *Proc. Natl. Acad. Sci. U. S. A.* **104**, 20713–20718 (2007).
94. G. Xue, R. F. De Hont, E. Münck, L. Que Jr., Million-fold activation of the [Fe₂(μ-O)₂] diamond core for C–H bond cleavage. *Nat. Chem.* **2**, 400–405 (2010).
95. R. F. De Hont, G. Xue, M. P. Hendrich, L. Que Jr.; E. L. Bominaar, E. Münck, Mössbauer, electron paramagnetic resonance, and density functional theory studies of synthetic S = 1/2 Fe^{III}–O–Fe^{IV}=O complexes. Superexchange-mediated spin transition at the Fe^{IV}=O Site. *Inorg. Chem.* **49**, 8310–8322 (2010).
96. H. Zheng, Y. Zang, Y. Dong, V. G. Young Jr., L. Que Jr., Complexes with Fe^{III}₂(μ-O)(μ-OH), Fe^{III}₂(μ-O)₂, and [Fe^{III}₃(μ₂-O)₃] cores: structures, spectroscopy, and core interconversions. *J. Am. Chem. Soc.* **121**, 2226–2235 (1999).
97. Y. Dong, L. Que Jr.; K. Kauffmann, E. Münck, An exchange coupled complex with localized high-spin Fe^{IV} and Fe^{III} sites of relevance to cluster X of escherichia coli ribonucleotide reductase. *J. Am. Chem. Soc.* **117**, 11377–11378 (1995).
98. M. H. Lim, J.-U. Rohde, A. Stubna, M. R. Bukowski, M. Costas, R. Y. N. Ho, E. Münck, W. Nam, L. Que Jr., An Fe^{IV}=O complex of a tetradentate tripodal nonheme ligand. *Proc. Natl. Acad. Sci. U. S. A.* **100**, 3665–3670 (2003).
99. T. K. Paine, M. Costas, J. Kaizer, L. Que Jr., Oxoiron(IV) complexes of the tris(2-pyridylmethyl)amine ligand family: effect of pyridine α-substituents. *J. Biol. Inorg. Chem.* **11**, 272–276 (2006).
100. M. S. Seo, N. H. Kim, K.-B. Cho, J. E. So, S. K. Park, M. Clemancey, R. Garcia-Serres, J.-M. Latour, S. Shaik, W. A. Nam, A mononuclear non-heme iron(IV)-oxo complex which is more reactive than cytochrome P450 model compound I. *Chem. Sci.* **2**, 1039–1045 (2011).

101. L. M. Hoffart, E. W. Barr, R. B. Guyer, J. M. Bollinger Jr., C. Krebs, Direct spectroscopic detection of a C–H-cleaving high-spin Fe(IV) complex in a prolyl-4-hydroxylase. *Proc. Natl. Acad. Sci. U. S. A.* **103**, 14738–14743 (2006).
102. D. P. Galonic, E. W. Barr, C. T. Walsh, J. M. Bollinger Jr., C. Krebs, Two interconverting Fe(IV) intermediates in aliphatic chlorination by the halogenase CytC3. *Nat. Chem. Biol.* **3**, 113–116 (2007).
103. M. L. Matthews, C. M. Krest, E. W. Barr, F. H. Vaillancourt, C. T. Walsh, M. T. Green, C. Krebs, J. M. Bollinger Jr. Substrate triggered formation and remarkable stability of the C–H bond cleaving chloroferryl intermediate in the aliphatic halogenase, SyrB2. *Biochemistry* **48**, 4331–4343 (2009).
104. B. E. Eser, E. W. Barr, P. A. Frantom, L. Saleh, J. M. Bollinger Jr., C. Krebs, P. F. Fitzpatrick, Direct spectroscopic evidence for a high-spin Fe(IV) intermediate in tyrosine hydroxylase. *J. Am. Chem. Soc.* **129**, 11334–11335 (2007).
105. E. A. Hill, A. C. Weitz, E. Onderko, A. Romero-Rivera, Y. Guo, M. Swart, E. L. Bominaar, M. T. Green, M. P. Hendrich, D. C. Lacy, A. S. Borovik, Reactivity of an Fe^{IV}-oxo complex with protons and oxidants. *J. Am. Chem. Soc.* **138**, 13143–13146 (2016).

Acknowledgments: We thank K. M. Carsch, T. D. Harris, A. Nguyen, J. Martell, R. Murphy, J. L. Peltier, M. Qi, B. E. R. Snyder, D. X. Ngo, X. Shen, and Y. Yang for helpful discussions.

Funding: This research was supported by the U.S. Department of Energy Office of Basic Energy Sciences under award DE-SC0019992. Single-crystal x-ray diffraction data were collected at beamlines 11.3.1 and 12.2.1 of the Advanced Light Source at Lawrence Berkeley National Laboratory, a user facility supported by the U.S. Department of Energy, Office of Science, Office of Basic Energy Sciences, Chemical Sciences, Geosciences & Biosciences Division Heavy Element Chemistry Program under contract no. DE-AC02-05CH11231. Synchrotron powder x-ray diffraction data were collected on the 17-BM-B Beamline at the Advanced Photon Source, a U.S. Department of Energy Office of Science User Facility operated by Argonne National Laboratory. NRVs data was collected at beamline 3-ID-B at the Advanced Photon Source. Use of the Advanced Photon Source at Argonne National Laboratory was supported by the U.S. Department of Energy, Office of Science, Office of Basic Energy Sciences (contract no. DE-AC02-06CH11357). Work at the Molecular Foundry was supported by the Office of Science, Office of Basic Energy Sciences, U.S. Department of Energy (contract no. DE-AC02-05CH11231). Instruments in the UC Berkeley College of Chemistry NMR facility are supported in part by NIH S10OD024998. EPR spectroscopic studies were funded by the National Institutes of Health (NIH 1R35GM126961 to R.D.B.). R.D.B. acknowledges support from the Miller Institute of Basic Research in Science, University of California, Berkeley. The computing cluster at the Molecular Graphics and Computation Facility at UC Berkeley is supported by NIH S10OD023532. The Fe K β XES measurements were carried out at the PINK beam line at the BESSY II electron storage ring operated by the Helmholtz-Zentrum Berlin für Materialien und Energie. D.J.S., S.P., E.B., D.A.P., S.D. and F.N. acknowledge the Max-Planck-Gesellschaft for funding. J.B. acknowledges the Deutsche Forschungsgemeinschaft for a Postdoctoral Research Fellowship. R.C.R. acknowledges the NASA Space Technology Graduate Research Opportunities fellowship. J.O. acknowledges the National Institute of General Medical Sciences for a Postdoctoral Research Fellowship under award F32GM143925. V.C. and M.V. acknowledge the

Italian Ministry of University and Research for a Ph.D. fellowship awarded to M.V. and funding through PRIN2017 program (Project “Moscato” n° 2017KKP5ZR_004).

Author contributions: K.H., J.B., and J.R.L. formulated the project. K.H. and J.B. synthesized the materials. J.B. and K.H. collected and analyzed reactivity study data. K.H. and J.B. collected and analyzed the gas adsorption data. H.K., J.W.T., and A.B.T. collected and analyzed the single-crystal x-ray diffraction data. H.Z., H.M., X.L., and J.A.R. collected and analyzed the solid-state NMR spectra. D.J.S. collected the applied-field Mössbauer data. D.J.S., K.H., J.B., K.R.M., F.G., G.J.L. and F.N. analyzed the data. D.J.S. and E.B. collected and analyzed the MCD data. K.C. and R.D.B. collected and analyzed EPR data. C.D. and J.J.U. collected and analyzed the EDX data. Z.Z. collected and analyzed the thermogravimetric analysis data. J.G.P. collected and analyzed the magnetic susceptibility data. H.Z.H.J., K.H., and J.B. collected and analyzed the IR spectra. M.V.P., H.Z.H.J., K.H., J.B., J.O., M.V., and V.C. collected and analyzed the PXRD data. J.B., K.H., E.E.A., J.Z., M.Y.H., and B.L. collected and analyzed the NRVS data. K.H., J.B., R.C.R., F.G., and G.J.L. collected and analyzed the Mössbauer spectroscopy data. J.B., K.H., D.A.P., and F.N. performed the electronic structure calculations and analyzed the results. S.P. and S.D. collected and analyzed the Fe K β XES data. K.H., J.B., K.R.M. and J.R.L. wrote the manuscript, and all authors contributed to revising the manuscript.

Competing interests: The University of California, Berkeley has applied for a patent (International application no. PCT/US23/70362) on the synthesis of the iron containing metal–organic frameworks and their reactivity with hydrocarbon substrates in the presence of dioxygen, on which J.B., K.H., and J.R.L. are listed as coinventors.

Data and materials availability: The supplementary materials contain complete experimental and spectral details for all new compounds reported herein. Single-crystal x-ray diffraction data have been made available free of charge from the Cambridge Crystallographic Data Centre under reference numbers CCDC 2166411 and 2166412. Powder x-ray diffraction and iron K β x-ray emission spectroscopy data are deposited in Dryad (<https://doi.org/10.5061/dryad.wh70rxwtp>).

Supplementary Materials

Materials and Methods

Supplementary Text

Figs. S1 to S71

Tables S1 to S17

References (49–105)

Data S1 and S2 (.cif)

Fig. 1. Design of a metal–organic framework mimic of taurine– α -ketoglutarate dioxygenase (TauD). (A) Illustration of the local structure of the mononuclear nonheme iron(II) sites in TauD and generation of the reactive high-spin Fe(IV)=O species (TauD-*J*) via oxidation with O₂ coupled with decarboxylation of the α -ketoglutarate co-substrate. **(B)** Illustration of the local coordination environment of the iron(II) sites in FeZn₄(prv)₄(btdd)₃ (R = CH₃) or FeZn₄(moba)₄(btdd)₃ (R =

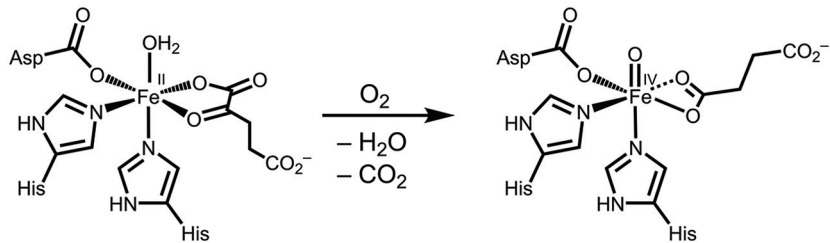
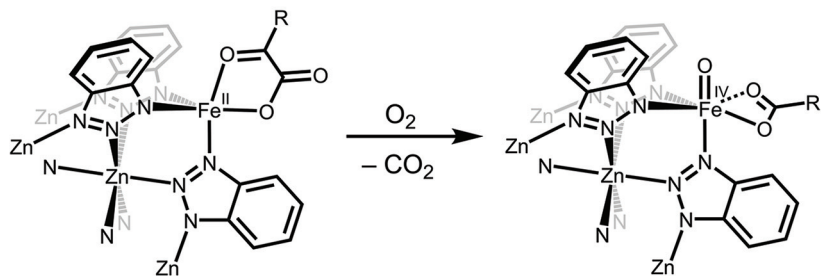
*t*Bu) and observed reactivity with O₂ at low temperatures to form an Fe(IV)=O species coordinated by acetate or pivalate formed via the decarboxylation of pyruvate (prv) or 3,3-dimethyl-2-oxobutyrate (moba), respectively. (C) (Left) Illustration of a cubic pore within FeZn₄(prv)₄(btdd)₃ derived using single-crystal x-ray diffraction data obtained for Zn₅(prv)₄(btdd)₃ (fig. S15B) and (right) expanded view of the truncated structure of a cluster node of the framework showing the nature of the pyruvate coordination, as supported by Mössbauer, magnetic circular dichroism, and nuclear resonance vibrational spectroscopies. Light blue, orange, red, blue, gray, and white spheres represent Zn, Fe, O, N, C, and H atoms, respectively.

Fig. 2. Investigation of reactivity between Fe_{1.8}Zn_{3.2}(prv)₄(btdd)₃ and O₂ using variable-temperature *in situ* DRIFTS. (A) Spectra obtained after dosing Fe_{1.8}Zn_{3.2}(prv)₄(btdd)₃ with 20 mbar of O₂ at 100 K and gradually warming to 298 K (solid lines). The peak at 2341 cm⁻¹ corresponds to CO₂ formed from the decarboxylation of pyruvate. This peak shifts to approximately 2275 cm⁻¹ when Fe_{1.8}Zn_{3.2}(1-¹³C-prv)₄(btdd)₃ is dosed with ¹⁸O₂ under the same conditions (dashed lines), consistent with formation of the isotopologue ¹³CO₂. (B) Spectra obtained as described in A showing the signature peaks for the iron(IV)=O species formed from the reaction between Fe_{1.8}Zn_{3.2}(prv)₄(btdd)₃ and O₂ (831 cm⁻¹) and Fe_{1.8}Zn_{3.2}(1-¹³C-prv)₄(btdd)₃ and ¹⁸O₂ (796 cm⁻¹). All data shown correspond to difference spectra obtained using the desolvated iron(II) frameworks as the background. Minor differences in the intensities of the absorption bands for the natural abundance and heavier isotopologue samples are likely due to differences in powder sample mass, sample distribution in the background matrix, and slight positioning differences in the infrared beam. (C) The reaction probed by DRIFTS, wherein for simplicity FeZn₄(1-¹³C-prv)₄(btdd)₃ is shown to react with ¹⁸O₂.

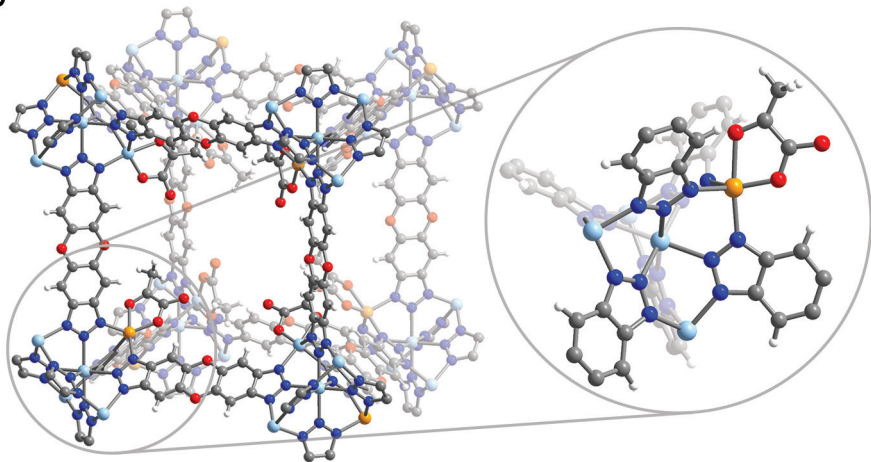
Fig. 3. *In situ* and variable-field Mössbauer spectra. (A) *In situ* Mössbauer spectra collected at 5 K for desolvated FeZn₄(prv)₄(btdd)₃ before and after dosing with 300 mbar of O₂ at 100, 125, and 150 K. All spectra were fit with a minimum number of symmetric quadrupole doublets, all of which have the same linewidth for a given spectrum (see fig. S22 for a timeline of the *in situ* dosing experiment). Green, blue, and dark red subspectra, respectively, are consistent with iron(II), iron(III), and iron(IV) species. (B) Variable magnetic field Mössbauer spectra collected at 1.7 K and the indicated fields for a sample of FeZn₄(moba)₄(btdd)₃ that had been dosed with 100 mbar of O₂ at 100 K, held for 2 h at 200 K and subsequently dosed with 200 mbar of O₂ at 100 K and then warmed again at 200 K for 2 h. Green, blue, dark red solid, and dark red dotted subspectra, respectively, were modeled as *S* = 2 iron(II), *S* = 5/2 iron(III), isolated *S* = 2 Fe(IV)=O species, and *S* = 0 species arising from antiferromagnetic coupling between Fe(IV)=O species within the same node. The spectra were modeled as described in the main text to extract *D* = 12.7(6) cm⁻¹ and *A*_{iso} = -16.4 T for the uncoupled Fe(IV)=O species (see table S13). Note, the width of the spectral splitting for the red trace at 7 T is smaller than has been observed for other *S* = 2 Fe(IV)=O species in the literature (~5 versus ~8 mm/s, respectively) (6, 17, 33). However, as demonstrated for another *S* = 2 Fe(IV)=O complex (34), a spectral splitting of about 5 mm/s can be observed if the hyperfine parameters are smaller than the isotropic Fermi-contact contribution of ~21 T, as it is the case for FeZn₄(moba)₄(btdd)₃ (see also fig. S36).

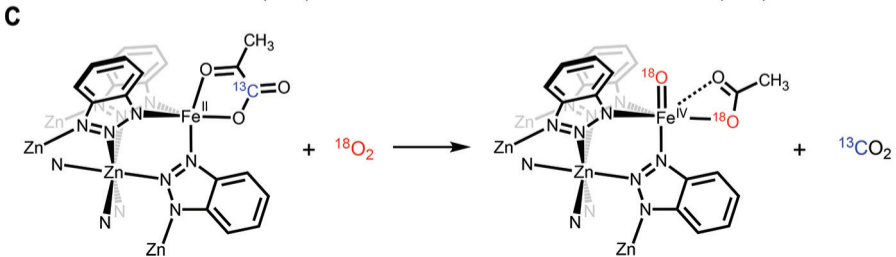
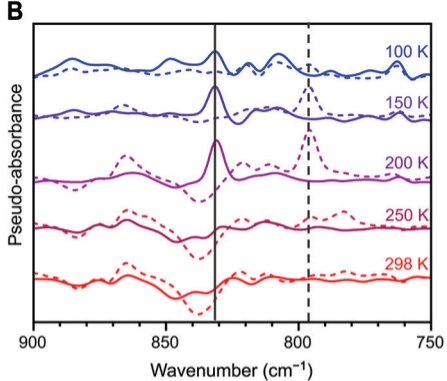
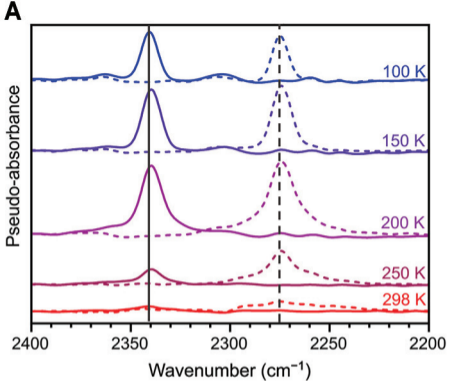
Fig. 4. Nuclear resonance vibrational spectroscopy (NRVS). (A) Iron partial vibrational density of states (PVDOS) distribution of ⁵⁷Fe-enriched, desolvated FeZn₄(prv)₄(btdd)₃ from NRVS data

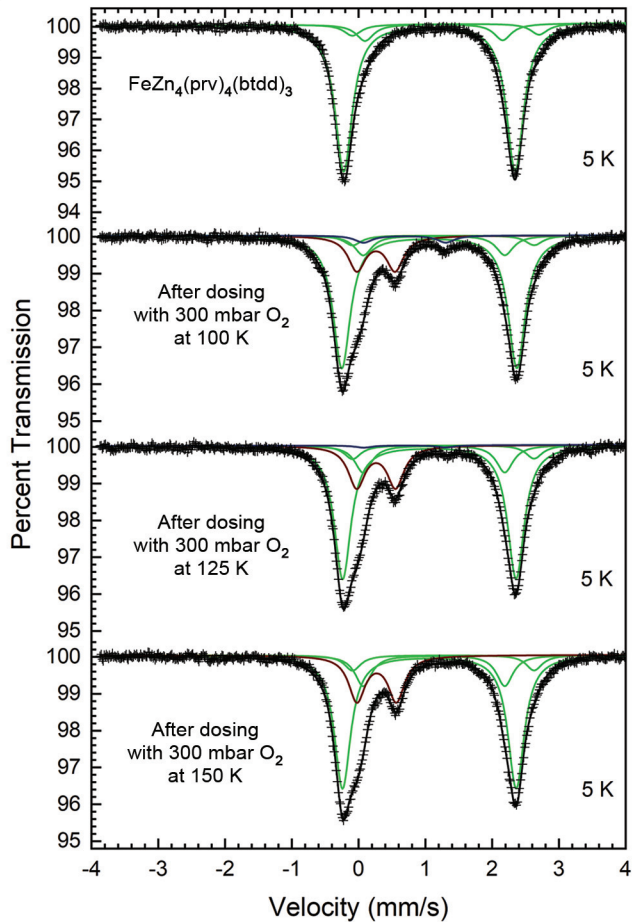
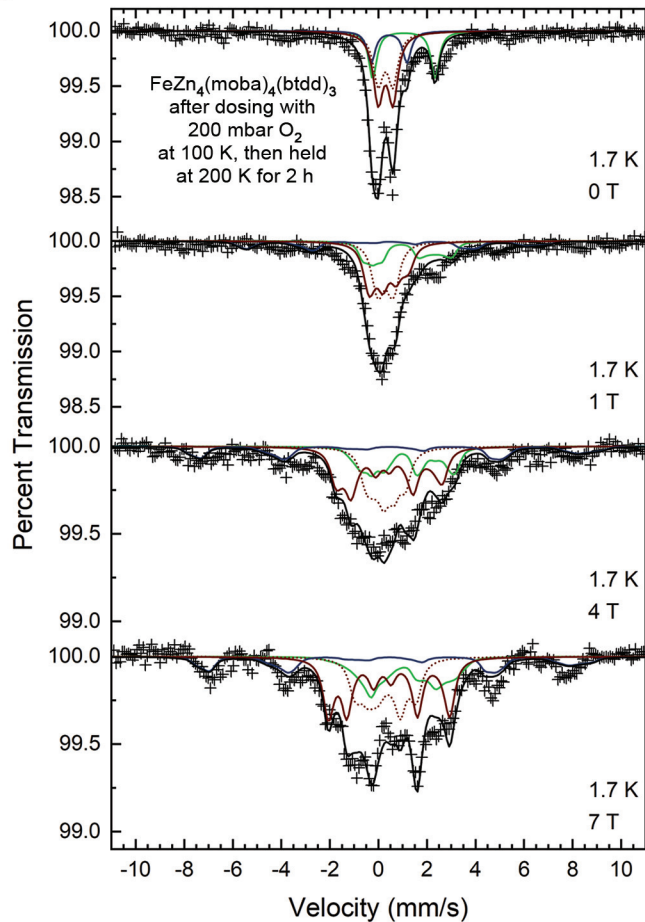
5 collected at ~ 100 K (green) and DFT computed Fe PVDOS for $\text{FeZn}_4(\text{prv})_4(\text{bta})_6$ (dark gray). **(B)** Iron PVDOS distribution of ^{57}Fe -enriched, desolvated $\text{FeZn}_4(\text{prv})_4(\text{btdd})_3$ obtained from NRVS data collected at ~ 100 K after dosing with 200 mbar of O_2 at 163 K (dark red) and DFT computed PVDOS distribution for $\sim 70\%$ $\text{FeZn}_4(\text{prv})_4(\text{bta})_6$ and $\sim 30\%$ of $\text{Fe}(\text{O})(\kappa^2\text{-OAc})\text{Zn}_4(\text{prv})_3(\text{bta})_6$ (dark gray). The inset shows a shift of the $\text{Fe}(\text{IV})=\text{O}$ vibration to lower wavenumbers ($\Delta = 34 \text{ cm}^{-1}$) when $^{18}\text{O}_2$ is used (light blue, see also fig. S46). Vertical lines indicate the individual vibrational transitions. **(C)** Assigned vibrational modes of $\text{FeZn}_4(\text{prv})_4(\text{btdd})_3$ and the O_2 -dosed framework.

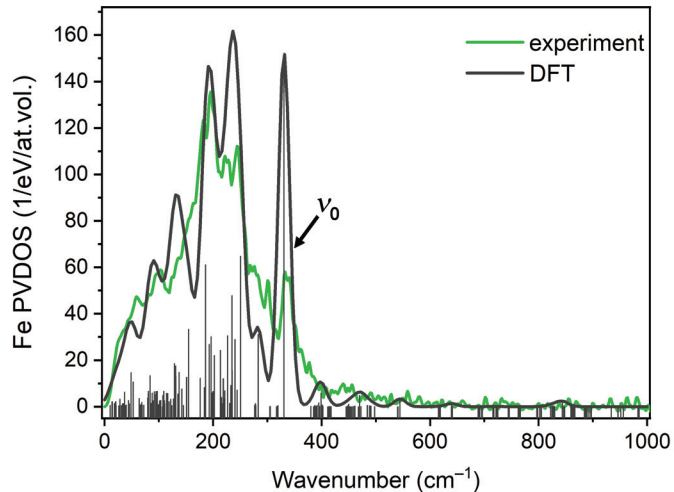
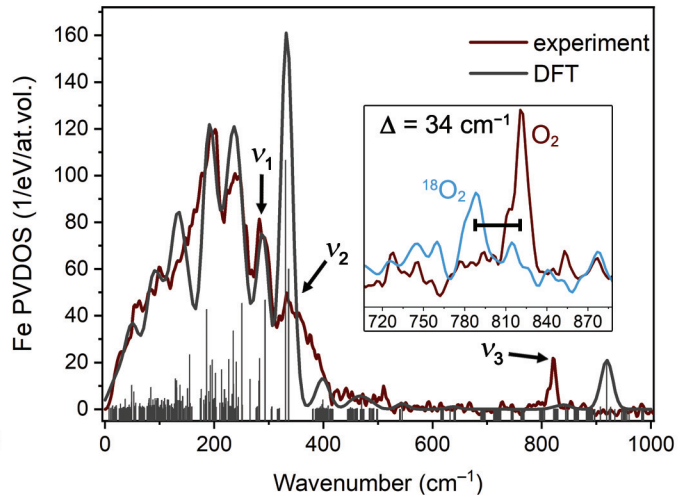
A**B**

R = CH₃ (prv), *t*Bu (moba)

C



A**B**

A**B****C**